Higher Order Liquid Crystalline Structure in Low-Polydispersity DEH-PPV

Bradley D. Olsen,[†,‡] Sung-Yeon Jang,[†,‡] Jan M. Lüning,[§] and Rachel A. Segalman*[,†,‡]

Department of Chemical Engineering, University of California, Berkeley, California 94720, and Materials Science Division, Lawrence Berkeley Laboratory, and Stanford Synchrotron Radiation Laboratory, P.O. Box 20450, Stanford, California 94309

Received January 23, 2006; Revised Manuscript Received April 11, 2006

ABSTRACT: Monodisperse, low molecular weight poly(2,5-di(2′-ethylhexyloxy)-1,4-phenylenevinylene) (DEH-PPV) demonstrates significantly better structural order than polydisperse PPVs. Since optical and electrical properties of polymer electronics are closely related to the structure and morphology of the active layer, morphological control is important for the fabrication of PPV-based devices. Soluble, monodisperse DEH-PPVs with a range of molecular weights showed a sequence of transitions through crystalline, smectic, nematic, and isotropic phases upon heating, and the transition temperatures increased sharply with increasing molecular weight. The layer spacing of the smectic phase is in good agreement with the length of a PPV molecule. The Maier−Saupe parameter for this polymeric system is estimated, and both energetic and entropic contributions are found to be important in describing the liquid crystalline interaction. Thin films revealed that the PPV molecules ordered into thermally stable layers a single molecule thick. The layers arranged into grains that were aligned by shearing. The orientation of molecules within the aligned layers was characterized by polarization-dependent X-ray absorption spectroscopy, and the PPV molecular axis was found to align parallel to the shear direction while the layers aligned perpendicular to the shear direction. Low polydispersity is critical to forming these types of highly ordered structures, and an analogous PPV sample with polydispersity greater than 5 does not form smectic layers.

Introduction

The mesoscale order and grain structure in semiconducting polymers greatly affect the electrical properties of optoelectronic devices[1−3] such as LEDs,[4−6] photovoltaics,[7,8] photodiodes,[9] and lasers.[10,11] Processing conditions[12−17] affect the film morphology, crystalline structure, molecular orientation, and resulting device properties. Polydispersity also has a large effect on polymer LED performance,[18] with devices incorporating low-polydispersity poly(phenylenevinylenes) (PPVs) having efficiencies greater than those of devices using high-polydispersity PPVs. An underlying structural and thermodynamic basis for the observed morphological dependencies on chemistry, processing, and polydispersity would help to improve the development of efficient PPV-based optoelectronic devices.

The structure of semiconducting polymers is governed to a large extent by the rigid nature of their π-conjugated backbones, which promote the formation of liquid crystalline phases. The effect of polydispersity on liquid crystalline polymers has been investigated using thermotropic polyesters.[19] Crystalline melting and nematic−isotropic (NI) transition temperatures both increase rapidly with molecular weight for short polymers, and a plateau value is reached at high molecular weights.[19] The width of the nematic region also grows with increasing molecular weight. For polydispersities greater than 1.6, the NI transition spreads into a coexistence region that widens as polydispersity is increased.[19] Smectic phases in polydisperse polymers are relatively rare, and in most cases smectic layers form between mesogenic monomers within the polymer chain. Recently, several authors have prepared monodisperse or nearly monodisperse polypeptides[20,21] and helical polysiloxanes[22] that have demonstrated smectic phases where the smectic layer spacing is equal to the length of a single polymer molecule. Low polydispersity is critical to the formation of these phases since disorder in chain length disrupts the formation of a single layer thickness.[20]

Liquid crystalline polymers are often side chain functionalized with long alkyl side groups to increase solubility or improve thermal properties, and the phase behavior of these polymers has been modeled using hairy rod theories.[23,24] The side groups act as bound solvent,[25] lowering transition temperatures and increasing thermal processability. Segregation of the side groups and the main chains is predicted to cause ordering into layers with a thickness close to the molecular diameter;[24] this type of layering has been experimentally observed in several systems.[26−29] Crystal structures are available for solubilized PPVs with short (methyl, methoxy, ethoxy) side chains,[30,31] and the effects of longer linear alkyl[25,32] and alkoxy[28,29,33−36] side chains on the structure and thermal properties have also been explored. At ambient temperatures most PPVs are semicrystalline, and the crystalline structure shows a strong dependence on the solubilizing side chain. Molecular dynamics simulations of poly(2-methyloxy-5-ethylhexyloxyphenylenevinylene) (MEH-PPV) and poly(2,5-dioctyloxyphenylenevinylene) (DOO-PPV) suggest that the chains are elliptically helical with phenyl ring orientations correlated over only 2−4 rings.[37] MEH-PPV films form polycrystalline domains where each domain is composed of a layered structure of coplanar MEH-PPV chains,[38,39] and the chains pack into fibrilar structures in the bulk.[29] DOO-PPV also forms semicrystalline fibrilar structures in the bulk,[28] and crystallites are oriented preferentially with the chain axis parallel to the substrate in thin films.[34] The melting and liquid crystalline clearing temperatures of PPVs with linear alkoxy side chains decrease as the side chain length is increased,[33,35] although in

† University of California, Berkeley.
‡ Lawrence Berkeley Laboratory.
§ Stanford Synchrotron Radiation Laboratory.
* Corresponding author: e-mail segalman@berkeley.edu.

10.1021/ma060164l CCC: $33.50
Published on Web 06/01/2006

Scheme 1. Chemical Structure of DEH-PPV

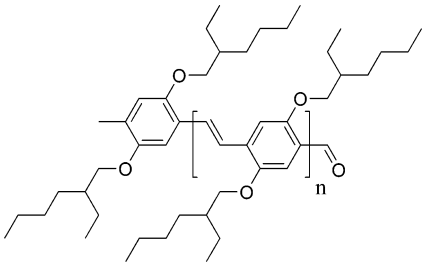

Table 1. PPV Molecular Weights (g/mol) and Polydispersities

polymer	M_n(NMR)	PS equiv M_n(GPC)	PS equiv PDI(GPC)
PPV-4.4	3400	4400	1.17
PPV-4.6	3500	4600	1.19
PPV-5.2	4100	5200	1.06
PPV-6.0	5100	6000	1.07
PPV-6.3	5600	6300	1.09
PPV-10.9		10900	1.08
PPV-polydisperse		16800	5.38

many cases the structures and phase transitions show strong thermal history effects.[32,33,35,36] While this prior work has explored many materials, the specific effects of molecular shape and polydispersity on structure and thermodynamics remain unclear.

This study focuses on understanding the bulk liquid crystalline behavior of PPVs with low polydispersity and how liquid crystallinity affects their behavior in thin films. We perform a detailed study of the structure and thermodynamics of low-polydispersity, low molecular weight poly(2,5-di(2′-ethylhexyloxy)phenylenevinylene) (DEH-PPV) and quantify the liquid crystalline behavior in terms of the Maier−Saupe theory. DEH-PPV is chosen as a model PPV due to its thermal processability, solubility in many common solvents, and ease of synthesis. The impact of molecular weight and film thickness on both the micron scale morphology and nanoscale liquid crystalline structure of thin films is investigated. Aligned films are prepared by rubbing, and the alignment of PPV molecules within nanoscale structures is studied. The behavior of the monodisperse PPVs is compared to that of a high polydispersity sample to elucidate the specific effects of polydispersity on the liquid crystalline structure of PPV.

Experimental Methods

Synthesis of Poly(2,5-di(2′-ethylhexyloxy)-1,4-phenylenevinylene) (DEH-PPV). DEH-PPV, shown in Scheme 1, was synthesized by Seigrist polycondensation as described previously.[40] The Seigrist polycondensation is a decelerating reaction that allows for the preparation of PPV with a narrow molecular weight distribution and containing only trans-linked units. For comparison, a polydisperse sample of DEH-PPV was synthesized using the Gilch method with a procedure similar to that previously described for MEH-PPV.[41] Number-average molecular weights were determined using NMR end-group analysis (Table 1). Polystyrene (PS) equivalent molecular weights were measured on a Waters 2690 GPC with a UV−vis detector operating at 254 nm (shown in Table 1), and specific PPVs are referred to by their PS equivalent number-average molecular weights throughout the text. The monodisperse PPVs had PS equivalent polydispersities ranging from 1.06 to 1.19, while the high-polydispersity PPV had a PS equivalent polydispersity of 5.38. Since the hydrodynamic volume of these rodlike molecules increases faster with increasing molecular weight than that of the polystyrene standards, these values tend to overestimate the molecular weight of the high molecular weight PPV tail. Therefore, the polystyrene equivalent polydispersity overestimates the actual PPV polydispersity and should be viewed as an upper limit on the true value.

Characterization. Samples for small-angle X-ray scattering (SAXS) and wide-angle X-ray scattering (WAXS) were prepared by pressing samples into 1 mm thick disks using a Carver press at 100 °C. Polymers were annealed under vacuum at 200 °C for 12 h to remove the nonequilibrium pressing effects, cooled slowly to room temperature, and sealed between Kapton windows. SAXS and WAXS experiments were performed on beamline 1-4 of the Stanford Synchrotron Radiation Laboratory (SSRL). The beamline was configured with an X-ray wavelength of 1.488 Å and focused to a spot size of ∼0.5 mm diameter. A single quadrant of the two-dimensional scattering pattern was collected on a CCD detector with a 100 mm diameter. The two-dimensional profiles were radially averaged and corrected for detector null signal, dark current, and empty cell scattering. SAXS profiles were converted to absolute intensities using a polyethylene standard calibrated at NIST, and WAXS profiles were left in arbitrary units.

Polarized optical microscopy (POM) samples were pressed between two glass slides and placed on an in situ argon-purged heat stage for optical imaging. Samples were annealed into the isotropic phase, cooled, and then heated at a rate of 0.2 °C/min to determine the liquid crystalline transition temperatures. Samples were also characterized by differential scanning calorimetry (DSC) using a TA Instruments 2920. Samples were heated to 250 °C at 10 °C/min to erase any thermal history, then cooled to 20 °C at 10 °C/min, and reheated to 300 °C at 5 °C/min.

Scanning force microscopy (SFM) samples were prepared by spin-coating films from toluene solution onto silicon wafers with a native oxide surface. Some samples were thermally treated by annealing under vacuum at 140 °C for 24 h and cooling slowly to room temperature. Aligned samples were prepared by gently rubbing as-cast films with a velvet cloth. Imaging was performed on a Digital Instruments MultiMode AFM operating in tapping mode.

Near-edge X-ray absorption fine structure (NEXAFS) measurements on rubbed PPV samples were performed at beamline 10-1 of the Stanford Synchrotron Radiation Laboratory (SSRL) with a resolution of ∼80 meV around the carbon K-edge. Spectra were obtained at X-ray incident angles ranging from 90° (normal to the sample surface) to 20° (grazing incidence), with a typical spot size of 0.2 mm × 1 mm in normal incidence. Measurements were taken with the electric field vector oriented both parallel and perpendicular to the rubbing direction. Absorption spectra were measured using Auger electron yield (AEY) and total electron yield (TEY) detectors[42] which sample the top surface layer of about 1−2 nm thickness and a thicker subsurface layer of about 5−10 nm, respectively. Spectra have been normalized to show the carbon K-edge absorption per atom, as described in the literature.[42−44] Absorption intensities were calculated using peak areas. To obtain the orientation distribution of molecular orbitals, intensity data were fit using a model for rubbed surfaces described in the literature.[44] This analysis[44] also accounts for the finite polarization degree of the incident X-ray beam (∼80% of the X-ray intensity with linear horizontal and 20% with linear vertical polarization).

Results and Discussion

Liquid Crystalline Phases of PPV Homopolymer. Low-polydispersity DEH-PPV demonstrates novel liquid crystalline phase behavior, and heating the polymers results in a series of transitions through crystalline, smectic, nematic, and isotropic phases. Optical micrographs of the liquid crystalline textures are shown in Figure 1, and DSC curves for all of the monodisperese polymers are shown in Figure 2. At ambient temperatures, all monodisperse polymers are solid and exhibit a smectic-like pattern under the optical microscope and very little optical transparency. Upon heating, the PPVs melt into a smectic phase, as indicated by an endothermic peak in the DSC. The enthalpy of this transition increases, and the transition

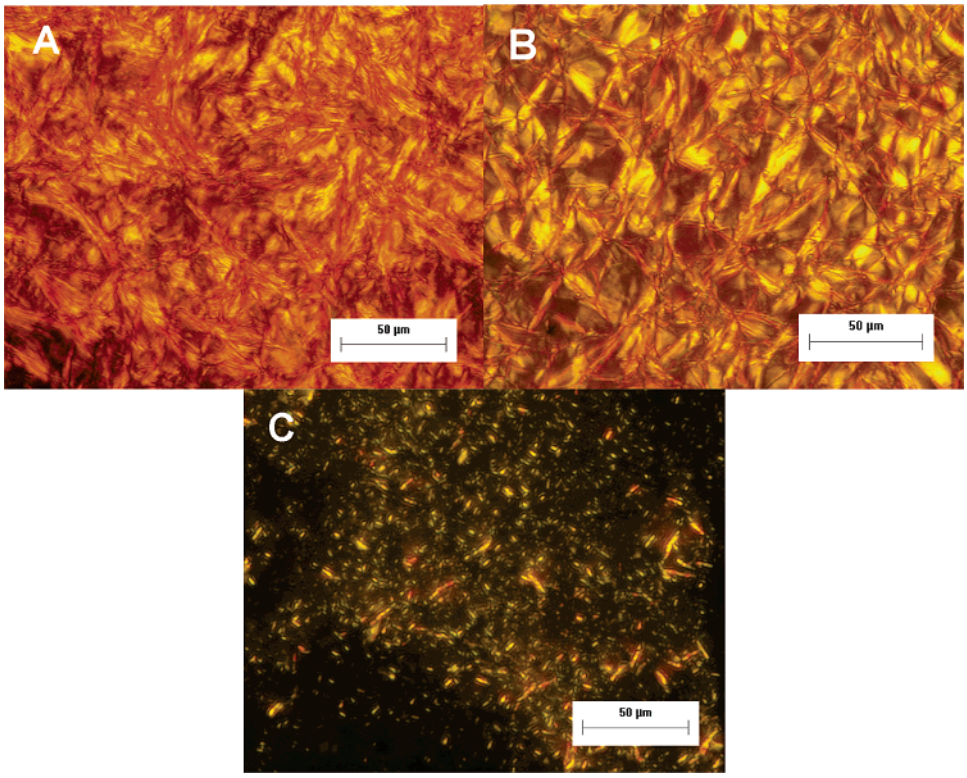

Figure 1. Polarized optical microscopy patterns of DEH-PPVs. At low temperatures, the DEH-PPVs show patterns characteristic of the crystalline or smectic phases, and at higher temperatures, the polymers exhibit patterns characteristic of a nematic phase. (A) PPV-6.0 at 200 °C in the smectic phase; (B) PPV-5.2 at 180 °C in the smectic phase; (C) PPV-4.6 at 190 °C in the nematic phase.

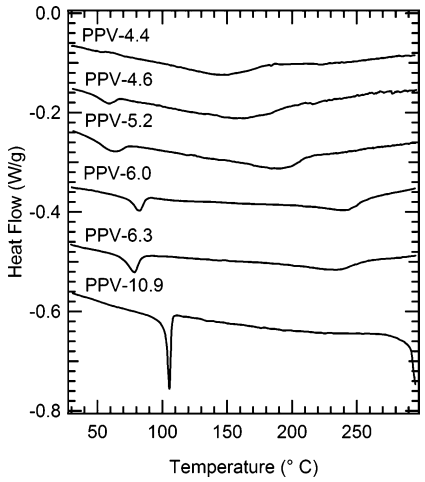

Figure 2. Differential scanning calorimetry (DSC) of DEH-PPV. DSC curves on heating show two transitions: a low-temperature endothermic transition and a higher temperature inflection point. The low-temperature transition is identified as the melting transition from crystalline to smectic, and the higher temperature transition is from smectic to nematic. The nematic−isotropic transition was not observed by DSC but was identified by polarized optical microscopy at temperatures above the smectic−nematic transition. Curves are offset for clarity.

becomes increasingly sharp with increasing molecular weight. Under the optical microscope, the polymers continue to exhibit a smectic texture and low transparency. Further heating results in a transition from a smectic to a nematic texture. At this point, the polymer becomes highly transparent, gains significant mobility, and flows readily, characteristic of the smectic to nematic (SN) transition.[45] The SN transition observed by optical microscopy corresponds to a broad inflection point in the DSC curves. This smectic phase is unique to the low-polydispersity samples; the high-polydispersity PPV melts directly into a nematic phase at 125 °C, and no inflection point is observed in the DSC. Kinetic effects in high molecular weight liquid crystals can make it difficult to grow the characteristic Schlieren textures exhibited by small molecule nematic liquid crystals.[46] Because of high defect densities, a polydomain or dense texture is observed in the monodisperse and polydisperse PPVs in the nematic region. Further heating results in the transition to a high temperature isotropic phase and the disappearance of the nematic polydomain texture. Because of the small enthalpy associated with the nematic−isotropic transition, it is not observed on the DSC. In general, the transition temperatures of the monodisperese PPVs increase with increasing molecular weight. However, PPV-6.0 and PPV-6.3 show an apparent small decrease in transition temperatures with increasing molecular weight. This is likely due to error inherent in using end-group analysis to estimate the number-average molecular weight.

Direct structural evidence in support of these liquid crystalline phase identifications was obtained using X-ray scattering. SAXS intensity patterns, shown in Figure 3, probe structure on the scale of the PPV polymer chain length. In three of the monodisperse polymers a weak peak was observed in the SAXS range, and the layer spacings corresponding to the peaks are shown in Table 2. For polymeric molecules, the width of the high electron density regions occupied by the molecules is much greater than the space between the smectic layers, so the lamellar form factor is near a minimum at the layer spacing peak,[47] producing a relatively low scattering intensity. Therefore, significant annealing is required to obtain the high degree of ordering necessary to observe the corresponding layer spacing peak. The experimentally observed layer spacings correspond to the polymer chain length calculated on the basis of crystallographic data,[48−53] implying that the mesogenic unit is the entire molecule. Heating of the lower molecular weight sample PPV-5.2 results in the disappearance of the peak near the temperature

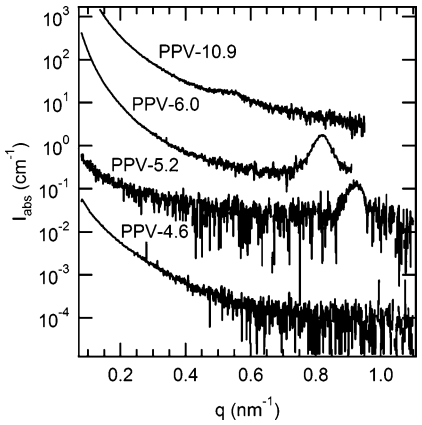

Figure 3. Small-angle X-ray scattering (SAXS) of DEH-PPV. SAXS shows peaks in three of the PPVs corresponding to spacing between the smectic layers. The layer spacing corresponds to the molecular length and increases with increasing molecular weight. Peaks have low intensity due to a minimum in the structure factor near the primary peak in highly asymmetric layered structures. Heating of the samples results in a decrease in peak intensity as the smectic−nematic transition is approached. The lowest molecular weight samples did not show smectic layers by SAXS, but the smectic−nematic transition was identified by optical microscopy and DSC. Curves are offset for clarity.

Table 2. Theoretical and Experimental Layer Spacings in PPVs.

polymer	calcd length (nm)	SAXS spacing (nm)	AFM spacing (nm)
PPV-4.6	6.6		8.3
PPV-5.2	7.6	6.8	
PPV-6.0	9.4	7.7	10.0
PPV-10.9		9.5	15.9

of the smectic−nematic transition, while for the other two polymers the smectic−nematic transition is above the experimentally accessible range of the SAXS. This suggests the formation of smectic phases where the layer spacing is equal to the molecular length, implying that the molecules are oriented perpendicular to the smectic layers and that there is no molecular folding. In the case of PPV 4-6, the slightly higher polydispersity may result in a diminished smectic peak in SAXS due to interfacial broadening. The high polydispersity PPV also demonstrates no layering peak, indicating that low polydispersity is required for the formation of this molecular smectic phase.

Although polydispersity has a large effect on smectic layering, the ethylhexyloxy side groups are the primary factor influencing rod−rod packing perpendicular to the rod axis. Figure 4 shows WAXS patterns for two polymers, PPV-6.0 and PPV-4.6, which exhibit crystalline, smectic, and nematic phases. The large peak at ~6.5 nm^{-1} corresponds to the spacing between molecular backbones, giving an estimated molecular diameter of 0.97 nm. Thermal expansion of the PPV causes the position of this peak to move slowly to lower q as temperature is increased. A series of additional reflections occur at larger wave vector transfers, and changes in these peaks correspond to changes between liquid crystalline phases. The higher molecular weight PPV (PPV-6.0) is crystalline below 80 °C; in this phase the rods lie on a square lattice in the plane perpendicular to the rod axis. The peaks are indexed for PPV-6.0 in Figure 4. The lower molecular weight sample PPV-4.6 does not form a well-ordered crystalline phase at low temperature as indicated by the low enthalpy of crystallization observed in DSC and the lack of well-defined peaks corresponding to the crystalline phase. However, for all of the higher molecular weight samples, the structure of the crystalline phase becomes independent of molecular weight and polydispersity, and the WAXS patterns are nearly identical to those of PPV-6.0. The achiral mixture of side groups in DEH-PPV is expected to result in much less side chain crystallinity than PPVs with linear alkyl side groups, and this may be reflected by the relatively weak intensity of the Bragg peaks from side chain interactions or $\pi-\pi$ interactions. It is noteworthy that no clear $\pi-\pi$ stacking peak is observed and that the melting temperature increases with increasing molecular weight, a behavior characteristic of molecular crystals and not semicrystalline or side group crystalline materials. However, crystallization of the molecule certainly involves the side groups, and so differentiating between these two types of crystallization is difficult.

The melting transition between 80 and 120 °C in PPV-6.0 is characterized by a change in the in-plane lattice on which the rods are arranged. The weak diffraction from side groups or the π system structure disappears, and the stronger diffractions characteristic of the rod lattice shift. Rod packing is still characterized by a single lattice parameter, and the secondary peak is intermediate between a square and hexagonal lattice. This suggests that the angle between lattice vectors changes slightly as the polymers melt, resulting in an oblique lattice above the melting transition. The new peaks are indexed for PPV-4.6 in Figure 4. The change in lattice structure observed at the melting transition is independent of molecular weight and polydispersity; the observation of the same structure in monodisperse and polydisperse PPVs indicates that rod−rod packing is independent of the formation of smectic layers. Since the smectic layer spacing is close to the molecular dimension and there is a great deal of in-plane ordering as evidenced by the series of peaks in WAXS, the smectic phase is suspected to be a higher order orthogonal smectic. Further heating disorders the lattice and results in a decrease in peak intensities as the polymer approaches the isotropic phase, as shown for PPV-4.6. This polymer transitions through a smectic phase and into a nematic phase above 160 °C, and in the high temperature nematic phase only a weak primary rod−rod spacing peak persists. The structure observed by WAXS is thermally reversible, and cooling the sample results in the reappearance of the low-temperature peaks in all of the phases.

The phase diagram for low-polydispersity DEH-PPV as a function of molecular weight is shown in Figure 5. Transitions between crystalline, smectic, nematic, and isotropic phases are observed across a wide range of molecular weights, and the transition temperatures increase with increasing molecular weights without reaching a plateau value. While coexistence between the nematic and isotropic phases is observed in many high polydispersity liquid crystalline polymers,[19] the low polydispersity of these materials results in narrow or nonexistent coexistence regions. The low polydispersity of the materials is the key factor in the formation of the highly ordered molecular smectic phase because layered packing requires a single characteristic length, and when the entire chain behaves as a single mesogen, this occurs only in monodisperse systems. The PPVs studied here are significantly shorter than those previously reported[54] and show no evidence of conformational defects such as bending on the molecular level. Instead, the relatively straight chains act as single mesogens to form layers. The degree of polydispersity that is tolerable in the molecular smectic phase remains unclear; however, it is apparent that a maximum exists, as highly polydisperse PPVs do not exhibit this type of order.

Calculation of Maier−Saupe Parameter in a Polymeric System. Maier−Saupe models are commonly used in mean-field theories of rodlike polymers and block copolymers to model liquid crystalline interactions.[55,56] The Maier−Saupe model conveniently parametrizes the free energy contributions

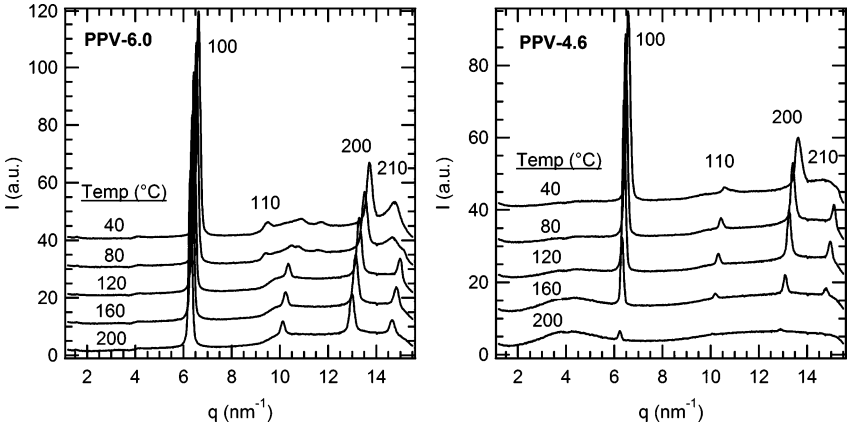

Figure 4. Wide-angle X-ray scattering (WAXS) of DEH-PPV. WAXS of the PPVs shows a series of peaks indicative of crystalline and smectic phases. The crystalline phase observed in PPV-6.0 at low temperatures shows many small resonances, and heating into the smectic phase causes four peaks to develop. These same peaks are observed in the smectic phase in PPV-4.6, and melting to the nematic phase in this polymer causes the peak intensities to decrease as the material loses order. Peak indexing for PPV-6.0 corresponds to the square lattice in the crystalline phase, where peaks at wavevector transfers of 1, $\sqrt{2}$, $\sqrt{4}$, and $\sqrt{5}$ indicate a square lattice. Partial crystallization of the side chains or relatively long-range interactions between the π systems of neighboring molecules account for the background scattering and weak peaks observed between 10 and 14 nm^{-1}. Peaks are indexed above the melting transition for PPV-4.6; both monodisperse and polydisperse polymers order on an oblique lattice in this region. Curves in both graphs are offset for clarity.

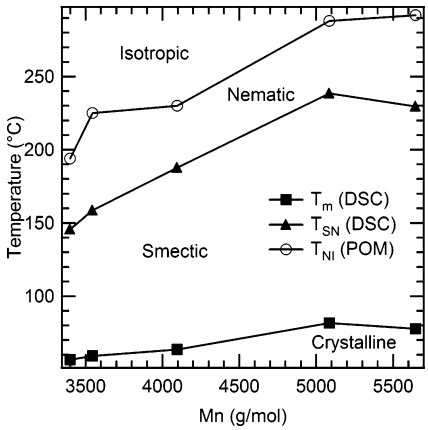

Figure 5. DEH-PPV phase diagram. DEH-PPV shows phase transitions from crystalline to smectic to nematic to isotropic on heating, and the transition temperatures increase with increasing molecular weight. The behavior of the melting and nematic−isotropic transitions is typical for liquid crystalline polymers, but the appearance of a smectic phase is unusual.

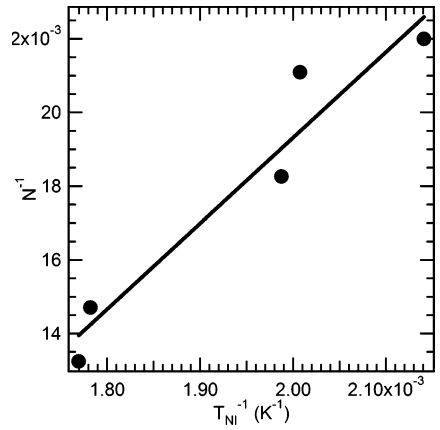

Figure 6. Fit to nematic−isotropic transition data to estimate Maier−Saupe parameter for DEH-PPV. Nematic−isotropic transition temperatures for DEH-PPV at a variety of molecular weights, determined by polarized optical microscopy, are fit to determine the form of the Maier−Saupe parameter. A form of the Maier−Saupe parameter $A/T + B$, analogous to the form of the Flory−Huggins interaction, results in a good fit to the experimental data.

that govern liquid crystallinity with a single parameter that is analogous to the Flory−Huggins parameter for isotropic polymer blends. Despite the utility of this parameter for predicting liquid crystalline phases in rodlike polymers and rod−coil block copolymers, measurements of its value are not available. Maier−Saupe models of rodlike polymers express the orientational component of the Hamiltonian that leads to nematic order as a spatially dependent quadratic function of the orientational order parameter S

$$\beta H = -\frac{\mu}{2\rho_0}\int \mathrm{d}\mathbf{r}\, \hat{\mathbf{S}}(\mathbf{r}):\hat{\mathbf{S}}(\mathbf{r}) \qquad (1)$$

where μ is the Maier−Saupe Parameter and ${\rho_0}^{-1}$ is the volume of a single rod segment. $\mathbf{S}$ is given by

$$\hat{\mathbf{S}}(\mathbf{r}) = \sum_{\alpha=1}^{n}\int_0^N \mathrm{d}s\, \delta[\mathbf{r} - (\mathbf{R}_\alpha + as\mathbf{u}_\alpha)]\left[\mathbf{u}_\alpha\mathbf{u}_\alpha - \frac{\mathbf{I}}{3}\right] \qquad (2)$$

where n is the number of molecules in the system, $\mathbf{R}_\alpha$ is the end of the rod corresponding to $s = 0$, N is the number of segments in the polymer, a is the length of a segment, and $\mathbf{u}$ is the dimensionless unit orientation vector. For a system of pure rods the partition function can be analytically calculated in the mean-field approximation. This calculation is performed in the Appendix, and it leads to the result that at the nematic−isotropic (NI) transition

$$(\mu N)_{\mathrm{NI}} = 6.811 \qquad (3)$$

This illustrates that the dimensionless parameter μN is the fundamental parameter governing liquid crystallinity in rodlike polymers, and it plays a role in the nematic−isotropic transition directly analogous to the Maier−Saupe parameter in small molecule liquid crystals.

The Maier−Saupe parameter is estimated for DEH-PPV based on a linear regression fit to NI transition data for polymers of various molecular weights, shown in Figure 6. Maier−Saupe theory for small molecule liquid crystals[45] predicts that μ is proportional to T^{-1}, and so a plot of N^{-1} vs T^{-1} should be linear with zero intercept. However, the data are fit much better by a form of the Maier−Saupe parameter analagous to the empirical form of the Flory−Huggins parameter, $A/T + B$. The line of

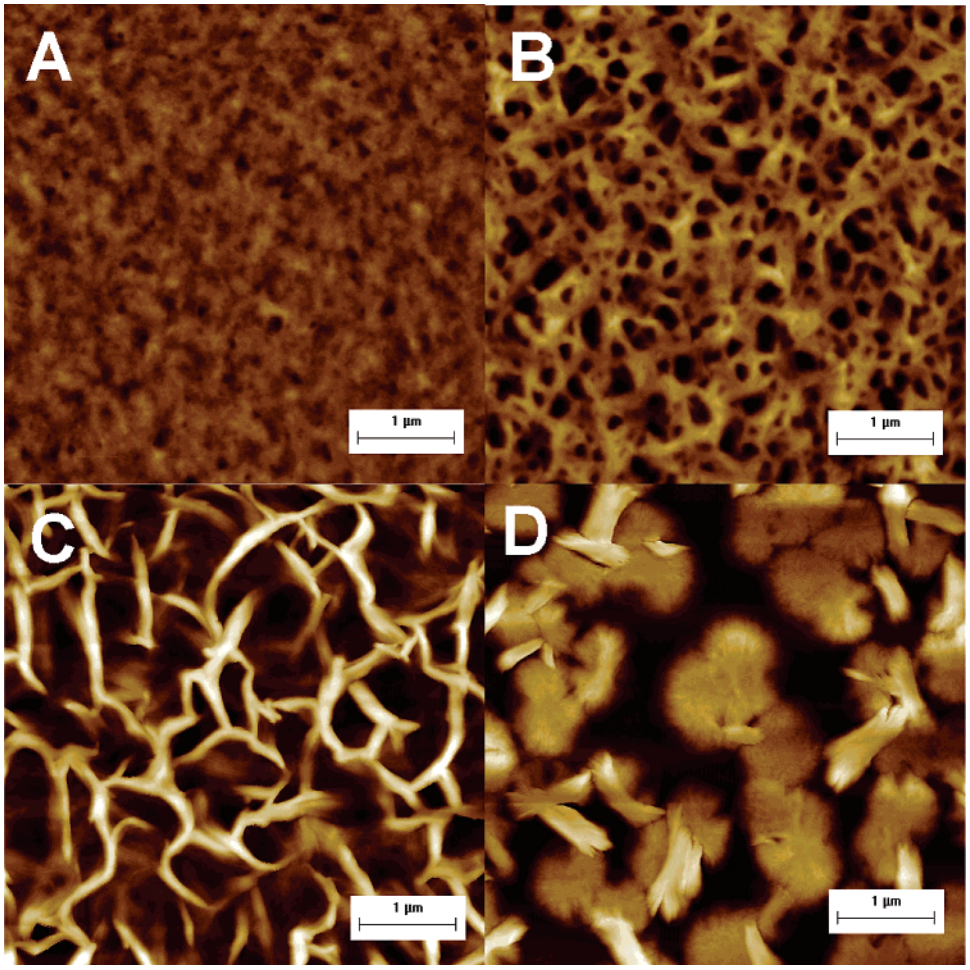

Figure 7. AFM height images of as-cast DEH-PPV Films. The structure of as-cast DEH-PPV films depends strongly on film thickness and the molecular weight of the polymer. Because of the strong tendency of these low-polydispersity PPVs to form liquid crystalline phases, phase separation occurs to form a polymer-rich lyotropic phase and a solvent-rich isotropic phase during spin-casting. The polymer-rich lyotropic phase solidifies, and the solvent-rich phase is depleted by evaporation, leaving a porous film structure behind. For low molecular weights and thinner films, the spin-casting is rapid enough to prevent micron-scale phase separation, but increasing molecular weight causes earlier onset of phase separation and thicker films cast more slowly, allowing large grain structures to develop. (A) PPV-4.6, 72 nm thick, height *z* range 50 nm; (B) PPV-4.6, 117 nm thick, height *z* range 100 nm; (C) PPV-6.0, 114 nm thick, height *z* range 150 nm; (D) PPV-10.9, 77 nm thick, height *z* range 250 nm.

best fit in Figure 6 gives an estimated Maier−Saupe parameter $\mu = 159/T - 0.189$. The disagreement between the small molecule form of the Maier−Saupe parameter and the experimental Maier−Saupe parameter in this system suggests that the Maier−Saupe parameter is capturing more than just enthalpic effects. In the small molecule theory the Maier−Saupe parameter is treated as an energy, but the constant term suggests the presence of entropic effects as well. The Flory−Huggins parameter for mixing, based in principle only on energetic contacts between molecules, also has an empirical form with both energetic and entropic contributions.[57] For DEH-PPV the entropic term is negative and the enthalpic term is positive, suggesting that enthalpic effects stabilize and entropic effects destabilize the lower temperature (nematic) phase, as is typical for most thermally induced phase transitions.

Micro- and Nanoscale Structure in DEH-PPV Thin Films. When the polymers are spun-cast to form films, lyotropic liquid crystalline states are kinetically trapped, resulting in the formation of micron scale polycrystalline domains, as shown in Figure 7. The lowest molecular weight polymer produces a flat surface when cast into thin films, while thicker films form a porous network-like morphology. Increasing the PPV molecular weight results in a change in grain shape and an increase in the size of the grains. There is less connectivity between grains and the network structure has much larger pores. At even higher molecular weight, large individual spherulitic grains coexist with a few elongated grains. The changes in film morphology with film thickness and molecular weight can be understood as kinetic effects resulting from spin-coating. Polymer and solvent separate into polymer-rich and solvent-rich phases during spin-casting due to the limited solubility of the polymer.[58] The polymer-rich phase has significant structural rigidity due to its liquid crystalline structure. As drying continues, the rigid polymer phase is unable to thin, so the solvent-rich phase is depleted from around the polymer-rich structures, leaving behind the observed PPV network morphologies and grain structures. The solubility of the polymers decreases as molecular weight increases, so phase separation will occur at lower polymer concentrations and the structures will have time to grow to larger sizes.

Annealing the samples results in significant structural rearrangement. Figure 8 shows AFM height and phase images of an annealed film of PPV-4.6. Annealing causes the formation of elliptical grains, visible as topographic features in the height image and ellipses with a positive phase shift in the phase image. We speculate that changes in modulus or adhesion with grain orientation would cause different grains to give a different phase signal.

Examination of the polymers on a smaller scale demonstrates that the microscale grains in all of the monodisperse PPVs are composed of nanoscale layers with a layer thickness comparable

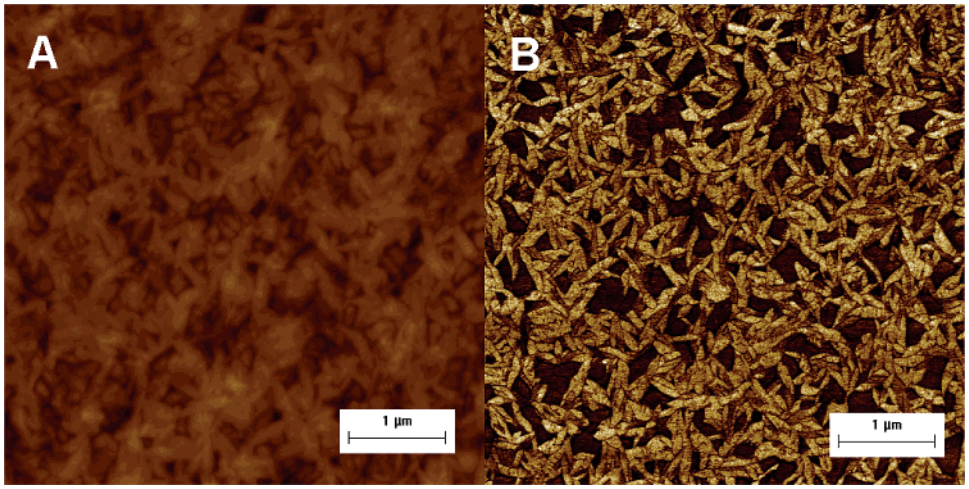

Figure 8. Thermal annealing of PPV-4.6 film. Annealing of the film shown previously in Figure 7A leads to growth of PPV grains as shown in the height image (A, *z* scale 100 nm). The phase image (B, *z* scale 30°) shows some grains appearing as light and others as dark due to mechanical differences related to grain orientations.

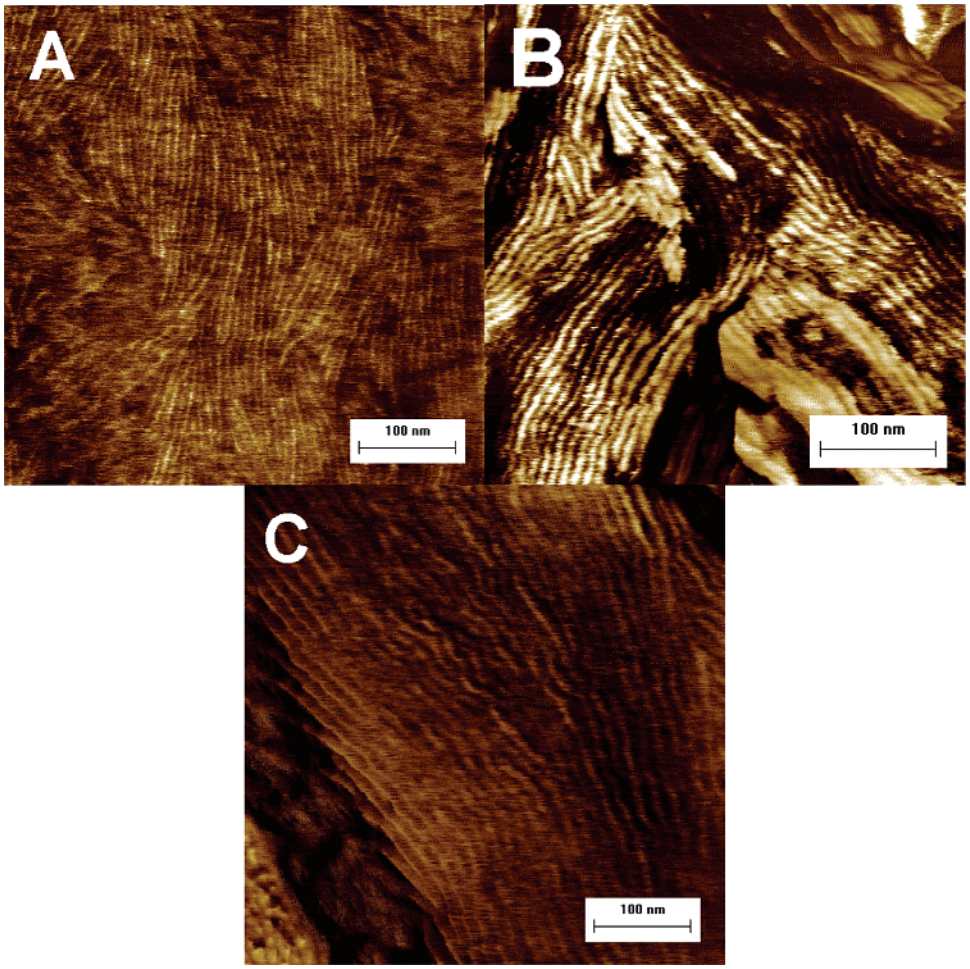

Figure 9. Layered structures in PPV thin films. As-cast PPV films show layered structures within the micron-sized grains for all molecular weights studied. The layers are stable after thermal annealing. Height images (not shown) are flat to within 2−3 nm, showing that the layers are not topographical features. Defects/grain boundaries between the layers are clearly observable. (A) PPV-4.6, 117 nm thick, phase *z* range 15°; (B) PPV-6.0, 114 nm thick, phase *z* range 60°; (C) PPV-10.9, 77 nm thick, phase *z* range 30°.

to the molecular length, as shown in Figure 9. The films are flat to within 2−3 nm, indicating that the layers are not topographical features and suggesting that the phase image is measuring properties directly related to the local density of molecules across the layers. The same nanoscale structures are observed in annealed films. The layers show strong correlation in alignment, and the number of aligned layers increases with increasing molecular weight. The layers also have a long persistence length, especially at higher molecular weights. The average widths of the needle structures are estimated in Table 2 from Fourier transforms of the SFM images. The layer spacings increase with increasing molecular weight of the polymers and are in reasonable agreement with the layer spacings measured by SAXS. Low polydispersity is critical to

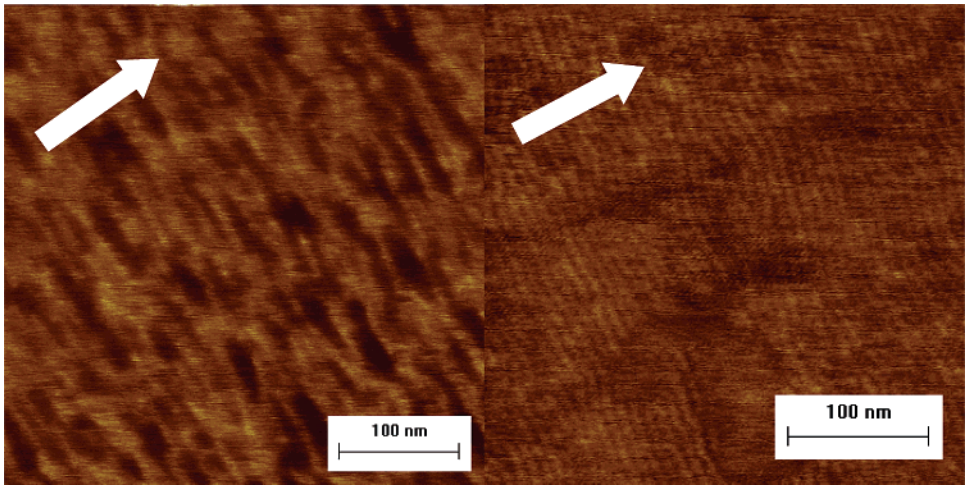

Figure 10. AFM of aligned PPV layers. Phase images of PPV-4.6 (left) and PPV-6.0 (right) after rubbing clearly show alignment of the PPV structures. Phase *z* range for both images is 30°. Arrows on the images indicate the rubbing direction, and the AFM shows alignment of the nanostructures perpendicular to the rubbing axis. The alignment direction is constant across the 1 cm wide sample.

the formation of these layered structures; layers are not observed in films of the high polydispersity PPV, consistent with the lack of a smectic phase in the bulk for this polymer.

Needlelike or rodlike structures have been previously observed in a few semiconducting polymers. DOO-PPV[28] and MEH-PPV[29] are thought to form a liquid crystalline phase of PPV with the backbones arranged in layers; the spacing between layers is governed by the size of the alkoxy side group. These structures aggregate into lamellae that are significantly larger than those observed in our polymers, having dimensions of ~20 nm. Chen et al.[28,29] used polymers with a high molecular weight and also high polydispersity, so their structural size is smaller than the length of a single molecule, indicating that molecules are folded within a single layer or traverse several lamellar aggregates. Kline et al. also observed needles in low molecular weight polythiophenes by AFM,[1] and they determined that the needlelike objects are polythiophene crystals. It appears that needlelike or layered structures may be a common feature of rodlike semiconducting polymers, but the nature of molecular arrangement varies greatly with chemical structure and polydispersity.

Alignment of PPV Nanostructures. Rubbing provides a useful tool for the preparation of PPV samples with a single molecular orientation for structural investigations, as shown by SFM images in Figure 10. The layered structures are aligned perpendicular to the rubbing direction, and the direction of alignment persists across the entire image. Rubbing produces long range orientational order as observed through the constant orientation direction of layers that extends across the entire sample (centimeter length scale). The nature of the aligned surface differs based on PPV molecular weight: PPV-4.6 is softer and has a lower molecular weight, so rubbing it forms a relatively disordered surface. Each individual lamellae is oriented perpendicular to the rubbing direction, but the lamellar positions are not strongly correlated with one another. PPV-6.0, having higher molecular weight and greater hardness, shows much more positional order after rubbing.

While orientation of the layered structures is clearly established by AFM, the orientation of molecules within the layers remains unclear. In particular, we wish to precisely determine the angle that the molecules make with respect to the layer normal. The average orientation of molecular orbitals within the molecules may be obtained by measuring the angle-dependent absorption of polarized X-rays. This provides quantitative information on the orientation of polymer chains[59] within the layered structures observed by AFM. Spectra are obtained for a range of X-ray incidence angles from 20° to 90° with the electric field vector oriented both parallel and perpendicular to the rubbing direction, as illustrated in Figure 11. In the parallel orientation the incident X-ray beam is oriented along the rubbing direction, with parallel orientation being defined as positive angles and antiparallel as negative angles. In the perpendicular orientation the X-rays are impinging perpendicular to the rubbing direction, with the positive *y*-direction in Figure 11 defining positive angles. Figure 12 shows the near-edge X-ray absorption fine structure (NEXAFS) spectra of PPV at two different X-ray incident angles with the incident X-ray beam parallel to the rubbing direction. The conjugated structure of PPV gives rise to a rich fine structure in the carbon K-edge absorption spectrum. On the basis of NEXAFS spectra for PPVs with different functional groups[60,61] and small model compounds,[42] peaks in the absorption spectrum can be identified. The π_1* peak at 285 eV shows a complex structure composed of a variety of overlapping absorption peaks. These originate from the various phenyl and vinyl carbon atoms of the conjugated backbone, which have small differences in transition energies. A π_2* peak is identified at 286 eV, and this peak partially overlaps with the σ_{C-H}* excitation at 288 eV. The σ_{C-C}* and $\sigma_{C=C}$* peaks are observed at 293 and 304 eV,

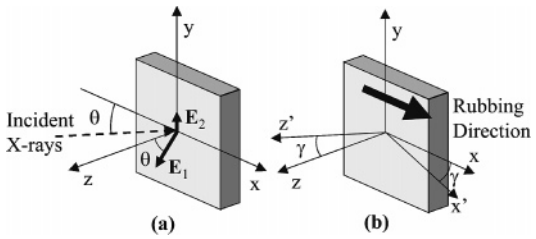

Figure 11. NEXAFS geometry. (a) The X-ray beam is incident to sample surface at a variable angle θ, where θ is positive when the beam is along the positive *x* and *y* directions and negative when the beam is along the negative *x* and *y* directions. The rubbing direction is in the positive *x* direction. The incident beam parallel or antiparallel to the rubbing direction is defined as parallel orientation, and the incident beam perpendicular to the rubbing direction is perpendicular orientation. The electric field vector of the X-rays is primarily polarized along $\mathbf{E}_1$, and the secondary component of the field vector is along $\mathbf{E}_2$. (b) A rotated coordinate system can be defined such that the axes x', y', and z' are the three principal axes of the molecular orbital distribution. This molecular coordinate system is rotated from the sample coordinate system by an angle γ about the $y = y'$ axis.

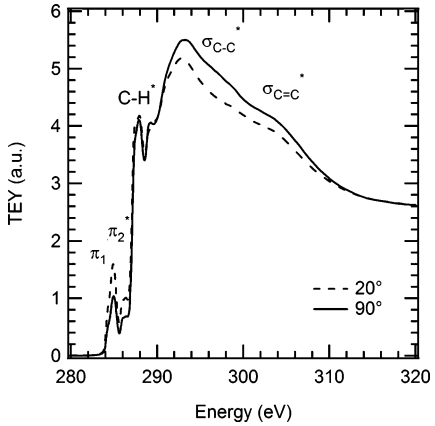

Figure 12. TEY spectra for PPV-6.0. TEY spectra are shown for incident X-rays parallel to the rubbing direction and the electric field making angles of 20° and 90° with the normal to the sample surface. Changes in the π^* and σ^* peaks clearly indicate the directionality of orbitals within the material. AEY spectra (not shown) have a similar shape to the TEY spectra. Peak locations are π_1^* 285 eV, π_2^* 286 eV, C−H* 288 eV, σ_{C-C}^* 293 eV, and $\sigma_{C=C}^*$ 304 eV.

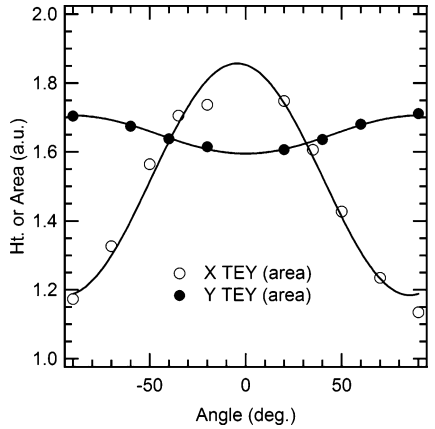

Figure 13. Fit to the π_1^* peak intensity to determine molecular orbital alignment in PPV-6.0. NEXAFS absorption is highest when the incident X-ray's electric field vector is aligned with an absorbing molecular orbital, so changes in absorption with changing X-ray incident angle can be used to calculate the orientational distribution of a molecular orbital. Parameters characterizing the molecular orientation distribution function are obtained by fitting the angle dependent intensity with periodic functions (solid lines).

respectively.[42] Changing from normal incidence (90°) to grazing incidence (20°) results in an increase in the π_1^* absorption at 285 eV and a decrease in the σ^* absorption, indicative of preferential alignment of the molecular orbitals.

The changes in the π_1^* intensity as a function of X-ray incidence angle can be analyzed to determine the orientation of the π-conjugated orbitals within the film. This spectral region is convenient for analysis because it is isolated in the NEXAFS spectrum, and the PPV orbitals contributing to the π_1^* resonance are all oriented perpendicular to the molecular axis. The π_1^* intensity is plotted as a function of incidence angle for both the parallel and perpendicular geometries in Figure 13. Parameters characterizing the molecular orientation function can be extracted from a fit[44] (solid lines in Figure 13) which shows overall excellent agreement with the experimental data. The pretilt angle γ, defined in Figure 11 as the angle between the fixed sample coordinates and the coordinates of the orbital's primary axes, and the orientation components f_x, f_y, and f_z along the orthogonal axes are given in Table 3. In addition, the derived X-ray polarization is listed. These data suggest that the π orbitals are preferentially aligned perpendicular to the rubbing direction (*x*-direction) with an azimuthal distribution of the orbitals about the rubbing axis. This indicates that the molecular axis is preferentially aligned parallel to the rubbing direction. The pretilt angle is very small, so the PPV backbones lie essentially parallel to the film surface. Prior studies suggest that the phenyl rings in PPV are tilted with respect to one another,[53,62,63] giving the molecules a helical shape. Such a twist in the PPV backbone would be consistent with an almost even distribution of π^* orbitals in the *y* and *z* directions.

Table 3. π-Orbital Distribution in PPV Films

polymer	detector	g	f_x	f_y	f_z	P
PPV-4.6	TEY	−0.028	0.185	0.416	0.399	0.72
	AEY	0.001	0.201	0.416	0.383	0.74
PPV-6.0	TEY	−0.078	0.196	0.417	0.387	0.75
	AEY	−0.013	0.229	0.417	0.353	0.73

Depth-dependent alignment of the polymers was measured using two electron detection modes. While Auger electron yield (AEY) samples only the top ∼1−2 nm of the film, total electron yield (TEY) probes ∼5−10 nm below the film surface.[44] Table 3 shows that the difference in measured molecular orientation distribution between the two detectors is minimal. This indicates that molecular alignment persists significantly deeper than the TEY sampling depth.

While individual PPV molecules are shown to align parallel to the rubbing direction by NEXAFS, the layers observed by AFM align perpendicular to the rubbing direction. Therefore, we infer that the layers are smectic layers of PPV molecules with the molecules oriented perpendicular to the layers. Comparison of the layer spacing to the molecular length suggests that each layer is a single molecule wide, and these observations in thin films are consistent with the tendency of the bulk materials to form smectic and layered crystalline phases where the molecule acts as a single mesogen.

Conclusions

The liquid crystalline structure and thermodynamics of low-polydispersity, low molecular weight DEH-PPV were investigated in both the bulk and thin films. Controlling the polydispersity of the PPV leads to the formation of highly ordered bulk liquid crystalline phases and layered morphologies in thin films that are not observed for polydisperse PPVs. For monodisperse PPVs a series of transitions through crystalline, smectic, nematic, and isotropic phases were observed. Transition temperatures increased with increasing molecular weight. The rodlike molecules order into layers a single molecule wide with the molecules parallel to the layer normal, resulting in a molecular smectic phase where the entire molecule acts as a single mesogen. This type of layered structure is unique to monodisperse liquid crystalline polymers since the monodisperse chain length directly translates into the monodisperse mesogen size required for layer formation. Data from the nematic−isotropic transition was also used to estimate the Maier−Saupe parameter in a polymeric system, and it was found to have an empirical form similar to the Flory−Huggins parameter, where both energetic and entropic considerations govern the transition behavior. The liquid crystalline properties of the polymers were reflected in thin films, where lyotropic phase separation during spin-casting results in network-like and large-grained film structures. The crystallites making up the spun-cast films of monodisperse PPV are composed of molecular-scale layers, while no layers are observed in a polydisperse PPV. Rubbing of the films causes the layers to align perpendicular to the rubbing direction, and the PPV molecules are aligned parallel to the rubbing direction, leading to the conclusion that the

monodisperse PPV grains are composed of smectic layers a single molecule wide.

Acknowledgments. We gratefully acknowledge support from the Department of Energy Office of Basic Energy Sciences through the Plastic Electronics Program at Lawrence Berkeley National Lab (LBNL). SAXS, WAXS, and NEXAFS experiments were performed at the Stanford Synchrotron Radiation Laboratory, a national user facility operated by Stanford University, supported by the Department of Energy, Office of Basic Energy Sciences. We gratefully acknowledge helpful discussions with Ron Oren and Ed Feng. We also thank John Pople and Nitash Balsara for use of equipment and experimental assistance. B. D. Olsen gratefully acknowledges the Fannie and John Hertz Foundation for a graduate fellowship.

Appendix. Solution for Maier−Saupe Parameter in Polymeric Field Theory

The field theory for rodlike polymers can be solved analytically in the mean-field approximation to determine the value of the Maier−Saupe parameter at the NI transition, and then a fit to the experimental data can be used to extract the functional dependence of the parameter on the thermodynamic variables of the system. While the traditional Maier−Saupe Hamiltonian is a sum over single molecules interacting with a mean-field order parameter, the field-theoretic Hamiltonian is an integral over a spatially dependent interaction, so the analytic calculation of the nematic−isotropic transition point is different in both theories. Following the formalism of Pryamitsyn and Ganesan,[55] we consider a system of n polymeric rods, each composed of N segments of length a and with a segmental volume ρ_0^{-1}. The density and orientational order parameters in the system are defined as

$$\text{density:} \qquad \hat{\rho}(\mathbf{r}) = \sum_{\alpha=1}^{n} \int_0^N \mathrm{d}s\ \delta[\mathbf{r} - (\mathbf{R}_\alpha + as\mathbf{u}_\alpha)] \tag{A1}$$

orientational order parameter:

$$\hat{S}(\mathbf{r}) = \sum_{\alpha=1}^{n} \int_0^N \mathrm{d}s\ \delta[\mathbf{r} - (\mathbf{R}_\alpha + as\mathbf{u}_\alpha)]\left[\mathbf{u}_\alpha\mathbf{u}_\alpha - \frac{\mathbf{I}}{3}\right] \tag{A2}$$

where $\mathbf{R}_\alpha$ is the end of the rod corresponding to $s = 0$ and the rod orientation vector, $\mathbf{u}$, is dimensionless. Then the partition function for the system can be written as

$$Z = \frac{1}{n!}\int D\mathbf{R}\ \mathrm{d}\mathbf{u}\ \delta[\hat{\rho}(\mathbf{r}) - \rho_0]\ \exp\left(\frac{\mu}{2\rho_0}\int d\mathbf{r}\ \hat{\mathbf{S}}(\mathbf{r}):\hat{\mathbf{S}}(\mathbf{r})\right) \tag{A3}$$

where μ is the Maier−Saupe parameter and the delta functional enforces the incompressibility constraint. The functional integral $D\mathbf{R}\ \mathrm{d}\mathbf{u}$ represents the summation over all possible end points and orientations of the rods. Using a Hubbard−Stratanovich transformation to introduce the potential field $\mathbf{M}$ conjugate to $\mathbf{S}$

$$\exp\left(\frac{\mu}{2\rho_0}\int \mathrm{d}\mathbf{r}\ \hat{\mathbf{S}}(\mathbf{r}):\hat{\mathbf{S}}(\mathbf{r})\right) = \int D\mathbf{M}\ \exp\left(-\frac{\rho_0}{2\mu}\int \mathrm{d}\mathbf{r}\ \mathbf{M}:\mathbf{M} + \int \mathrm{d}\mathbf{r}\ \mathbf{M}:\hat{\mathbf{S}}(\mathbf{r})\right) \tag{A4}$$

and interesting the delta functional identity in terms of the conjugate field π

$$\delta[\hat{\rho}(\mathbf{r}) - \rho_0] = \int D\pi\ \exp(-i\pi(\hat{\rho}(\mathbf{r}) - \rho_0)) \tag{A5}$$

allows the partition function to be transformed to

$$Z \propto \frac{1}{n!}\int D\mathbf{M}D\pi\ \times \exp\left(CV\ln Q + iC\int \mathrm{d}\mathbf{x}\ \pi - \frac{C}{2\mu N}\int \mathrm{d}\mathbf{x}\ \mathbf{M}:\mathbf{M}\right) \tag{A6}$$

where the equation has been nondimensionalized using $C = \rho_0(aN)^3/N$, the dimensionless system volume $V = V_{sys}/(aN)^3$, the dimensionless length $\mathbf{x} = \mathbf{r}/aN$, and the scaled contour variable $t = s/N$. The conjugate fields π and $\mathbf{M}$ are also scaled by a factor of N. The partition function for a single molecule interacting with the conjugate fields is

$$Q = \int \mathrm{d}\mathbf{x}\ \mathrm{d}\mathbf{u}\ \times \exp\left(-\int_0^1 \mathrm{d}t\left[i\pi(\mathbf{x} + t\mathbf{u}) - \mathbf{M}(\mathbf{x} + t\mathbf{u}):\left(\mathbf{uu} - \frac{\mathbf{I}}{3}\right)\right]\right) \tag{A7}$$

In the mean-field approximation the Hamiltonian is approximated by its value at a saddle point to give the self-consistent equations for the potential fields:

$$\begin{aligned} \phi(\mathbf{x}) &= 1 \\ \mathbf{M}(\mathbf{x}) &= \mu N\mathbf{S}(\mathbf{x}) \end{aligned} \tag{A8}$$

where the first self-consistent equation represents the incompressibility constraint. The orientational order parameter can be evaluated from the single molecule partition function as

$$\mathbf{S}(\mathbf{x}) = \frac{V}{Q}\int_0^1 \mathrm{d}t\int \mathrm{d}\mathbf{u}\left(\mathbf{uu} - \frac{\mathbf{I}}{3}\right)\times \exp\left[-\int_0^1 \mathrm{d}t'\left[i\pi(\mathbf{x} + t'\mathbf{u} - s\mathbf{u}) - \mathbf{M}(\mathbf{x} + t'\mathbf{u} - s\mathbf{u}):\left(\mathbf{uu} - \frac{\mathbf{I}}{3}\right)\right]\right] \tag{A9}$$

To simplify the theory, we consider uniaxial alignment of the molecules along the z-axis such that $M_{11} = M_{22} = -0.5M_{33}$ and $M_{12} = M_{21} = M_{13} = M_{31} = M_{23} = M_{32} = 0$. In addition, we assume that the thermally averaged orientational order parameter and conjugate field are spatially invariant. These two assumptions and the incompressibility constraint allow the expressions for Q and $\mathbf{S}$ to be simplified to

$$\begin{aligned} Q &= V\int \mathrm{d}\mathbf{u}\ \exp[M_{11}(1 - 3\cos^2\theta)] \\ \mathbf{S} &= \frac{V}{Q}\int \mathrm{d}\mathbf{u}\left(\mathbf{uu} - \frac{\mathbf{I}}{3}\right)\exp[M_{11}(1 - 3\cos^2\theta)] \end{aligned} \tag{A10}$$

Considering only S_{33} and substituting in for M_{11} using eq A8

$$S_{33} = -2S_{11} = \frac{\int_0^{2\pi}\int_0^{\pi}\mathrm{d}\phi\ \mathrm{d}\theta\ \sin\theta\left(\cos^2\theta - \frac{1}{3}\right)\exp[\mu NS_{11}(1 - 3\cos^2\theta)]}{\int_0^{2\pi}\int_0^{\pi}\mathrm{d}\phi\ \mathrm{d}\theta\ \sin\theta\ \exp[\mu NS_{11}(1 - 3\cos^2\theta)]} \tag{A11}$$

The roots of this equation may be identified numerically as a function of μN to find the equilibrium order parameter. The transition between nematic and isotropic phases occurs at $\mu N = 6.811$. Analagous to the small molecule Maier−Saupe theory, in the nematic phase there are two roots to eq A11: an isotropic solution $S_{33} = 0$ and an oriented solution $S_{33} > 0$. The nematic phase can be determined as the equilibrium phase based on free energy arguments.

The polymeric self-consistent field formalism is very similar to the Maier−Saupe theory developed for small molecules, where the single molecule partition function is represented as

$$Q_{MS} = \int d\mathbf{u} \exp\left[\frac{u_{MS}}{k_B T V_c^2} s \frac{1}{2}(3\cos^2\theta - 1)\right] \quad \text{(A12)}$$

where s represents the mean-field order parameter, which is given by

$$s = \frac{1}{2}\langle 3\cos^2\theta - 1\rangle = \frac{3}{2}S_{33} = -3S_{11} \quad \text{(A13)}$$

Examining the form of the Hamiltonian in each partition function, an analogy can be drawn between the polymeric and small-molecule Maier−Saupe parameters:

$$\mu N = \frac{3}{2}\frac{u_{MS}}{k_B T V_c^2} \quad \text{(A14)}$$

This analogy explains why the transition point is $u_{MS}/k_B T V_c^2 = 4.541$ in the small molecule theory but $\mu N = 6.811$ in the polymeric theory. Using data for the nematic isotropic transition, the Maier−Saupe parameter can then be estimated, analogous to the technique used with small molecule liquid crystals.[45]

References and Notes

(1) Kline, R. J.; McGehee, M. D.; Kadnikova, E. N.; Liu, J. S.; Frechet, J. M. J. *Adv. Mater.* **2003**, *15*, 1519−1522.
(2) Sirringhaus, H.; Wilson, R. J.; Friend, R. H.; Inbasekaran, M.; Wu, W.; Woo, E. P.; Grell, M.; Bradley, D. D. C. *Appl. Phys. Lett.* **2000**, *77*, 406−408.
(3) Winokur, M. J.; Chunwachirasiri, W. *J. Polym. Sci., Part B: Polym. Phys.* **2003**, *41*, 2630−2648.
(4) Burroughes, J. H.; Bradley, D. D. C.; Brown, A. R.; Marks, R. N.; Mackay, K.; Friend, R. H.; Burns, P. L.; Holmes, A. B. *Nature (London)* **1990**, *347*, 539−541.
(5) Friend, R. H.; Gymer, R. W.; Holmes, A. B.; Burroughes, J. H.; Marks, R. N.; Taliani, C.; Bradley, D. D. C.; Dos Santos, D. A.; Bredas, J. L.; Logdlund, M.; Salaneck, W. R. *Nature (London)* **1999**, *397*, 121−128.
(6) Gustafsson, G.; Cao, Y.; Treacy, G. M.; Klavetter, F.; Colaneri, N.; Heeger, A. J. *Nature (London)* **1992**, *357*, 477−479.
(7) de Boer, B.; Stalmach, U.; van Hutten, P. F.; Melzer, C.; Krasnikov, V. V.; Hadziioannou, G. *Polymer* **2001**, *42*, 9097−9109.
(8) Sariciftci, N. S.; Smilowitz, L.; Heeger, A. J.; Wudl, F. *Science* **1992**, *258*, 1474−1476.
(9) Granstrom, M.; Petritsch, K.; Arias, A. C.; Lux, A.; Andersson, M. R.; Friend, R. H. *Nature (London)* **1998**, *395*, 257−260.
(10) Hide, F.; DiazGarcia, M. A.; Schwartz, B. J.; Andersson, M. R.; Pei, Q. B.; Heeger, A. J. *Science* **1996**, *273*, 1833−1836.
(11) Tessler, N.; Denton, G. J.; Friend, R. H. *Nature (London)* **1996**, *382*, 695−697.
(12) Nguyen, T. Q.; Martini, I. B.; Liu, J.; Schwartz, B. J. *J. Phys. Chem. B* **2000**, *104*, 237−255.
(13) Inigo, A. R.; Chiu, H. C.; Fann, W.; Huang, Y. S.; Jeng, U. S.; Lin, T. L.; Hsu, C. H.; Peng, K. Y.; Chen, S. A. *Phys. Rev. B* **2004**, *69*.
(14) Nguyen, T. Q.; Schwartz, B. J.; Schaller, R. D.; Johnson, J. C.; Lee, L. F.; Haber, L. H.; Saykally, R. J. *J. Phys. Chem. B* **2001**, *105*, 5153−5160.
(15) Weir, B. A.; Marseglia, E. A.; Chang, S. M.; Holmes, A. B. *Synth. Met.* **1999**, *101*, 154−155.
(16) Schaller, R. D.; Snee, P. T.; Johnson, J. C.; Lee, L. F.; Wilson, K. R.; Haber, L. H.; Saykally, R. J.; Nguyen, T. Q.; Schwartz, B. J. *J. Chem. Phys.* **2002**, *117*, 6688−6698.
(17) Tan, C. H.; Inigo, A. R.; Hsu, J. H.; Fann, W.; Wei, P. K. *J. Phys. Chem. Solids* **2001**, *62*, 1643−1654.
(18) Menon, A.; Dong, H. P.; Niazimbetova, Z. I.; Rothberg, L. J.; Galvin, M. E. *Chem. Mater.* **2002**, *14*, 3668−3675.
(19) Chiellini, E.; Laus, M. In *Handbook of Liquid Crystals: High Molecular Weight Liquid Crystals*; Demus, D., Goodby, J., Gray, G. W., Spiess, H.-W., Vill, V., Eds.; Wiley-VCH: New York, 1998; Vol. 3, pp 26−51.
(20) Yu, S. J. M.; Conticello, V. P.; Zhang, G. H.; Kayser, C.; Fournier, M. J.; Mason, T. L.; Tirrell, D. A. *Nature (London)* **1997**, *389*, 167−170.
(21) Yu, S. J. M.; Soto, C. M.; Tirrell, D. A. *J. Am. Chem. Soc.* **2000**, *122*, 6552−6559.
(22) Okoshi, K.; Kamee, H.; Suzaki, G.; Tokita, M.; Fujiki, M.; Watanabe, J. *Macromolecules* **2002**, *35*, 4556−4559.
(23) Ballauff, M. *Macromolecules* **1986**, *19*, 1366−1374.
(24) Stepanyan, R.; Subbotin, A.; Knaapila, M.; Ikkala, O.; ten Brinke, G. *Macromolecules* **2003**, *36*, 3758−3763.
(25) Zhu, W.; Li, W. J.; Yu, L. P. *Macromolecules* **1997**, *30*, 6274−6279.
(26) Ballauff, M. *Angew. Chem., Int. Ed. Engl.* **1989**, *28*, 253−267.
(27) Watanabe, J.; Harkness, B. R.; Sone, M.; Ichimura, H. *Macromolecules* **1994**, *27*, 507−512.
(28) Chen, S. H.; Su, A. C.; Han, S. R.; Chen, S. A.; Lee, Y. Z. *Macromolecules* **2004**, *37*, 181−186.
(29) Chen, S. H.; Su, A. C.; Chou, H. L.; Peng, K. Y.; Chen, S. A. *Macromolecules* **2004**, *37*, 167−173.
(30) Resel, R.; Kiebooms, R.; Vanderzande, D.; Stelzer, F. *Monatsh. Chem.* **2001**, *132*, 433−440.
(31) Martens, J. H. F.; Marseglia, E. A.; Bradley, D. D. C.; Friend, R. H.; Burn, P. L.; Holmes, A. B. *Synth. Met.* **1993**, *55*, 449−453.
(32) Krebs, F. C.; Jorgensen, M. *Macromolecules* **2003**, *36*, 4374−4384.
(33) Bao, Z. N.; Chen, Y. M.; Cai, R. B.; Yu, L. P. *Macromolecules* **1993**, *26*, 5281−5286.
(34) Resel, R.; Tertinek, B.; Tasch, S.; Davey, A.; Blau, W.; Horhold, H. H.; Rost, H.; Leising, G. *Synth. Met.* **1999**, *101*, 96−97.
(35) Yu, L. P.; Bao, Z. N. *Adv. Mater.* **1994**, *6*, 156−159.
(36) Babudri, F.; Cicco, S. R.; Farinola, G. M.; Naso, F.; Bolognesi, A.; Porzio, W. *Macromol. Rapid Commun.* **1996**, *17*, 905−911.
(37) Yang, H. C.; Hua, C. Y.; Kuo, M. Y.; Huang, Q.; Chen, C. L. *ChemPhysChem* **2004**, *5*, 373−381.
(38) Jeng, U.; Hsu, C. H.; Sheu, H. S.; Lee, H. Y.; Inigo, A. R.; Chiu, H. C.; Fann, W. S.; Chen, S. H.; Su, A. C.; Lin, T. L.; Peng, K. Y.; Chen, S. A. *Macromolecules* **2005**, *38*, 6566−6574.
(39) Yang, C. Y.; Hide, F.; Diaz-Garcia, M. A.; Heeger, A. J.; Cao, Y. *Polymer* **1998**, *39*, 2299−2304.
(40) Olsen, B. D.; Segalman, R. A. *Macromolecules* **2005**, *38*, 10127−10137.
(41) Neef, C. J.; Ferraris, J. P. *Macromolecules* **2000**, *33*, 2311−2314.
(42) Stohr, J. *NEXAFS Spectroscopy*; Springer-Verlag: New York, 2003.
(43) Stohr, J.; Samant, M. G.; Cossy-Favre, A.; Diaz, J.; Momoi, Y.; Odahara, S.; Nagata, T. *Macromolecules* **1998**, *31*, 1942−1946.
(44) Stohr, J.; Samant, M. G. *J. Electron Spectrosc. Relat. Phenom.* **1999**, *99*, 189−207.
(45) Singh, S. *Phys. Rep.: Rev. Sect. Phys. Lett.* **2000**, *324*, 108−269.
(46) Noel, C. In *Handbook of Liquid Crystals: High Molecular Weight Liquid Crystals*; Demus, D., Goodby, J., Gray, G. W., Spiess, H.-W., Vill, V., Eds.; Wiley-VCH: New York, 1998; Vol. 3, pp 93−120.
(47) Roe, R.-J. *Methods of X-Ray and Neutron Scattering in Polymer Science*; Oxford University Press: New York, 2000.
(48) Capaz, R. B.; Caldas, M. J. *J. Mol. Struct.: THEOCHEM* **1999**, *464*, 31−38.
(49) Capaz, R. B.; Caldas, M. J. *Phys. Rev. B* **2003**, *67*.
(50) Zheng, G.; Clark, S. J.; Brand, S.; Abram, R. A. *J. Phys: Condens. Matter* **2004**, *16*, 8609−8620.
(51) Lagowski, J. B. *J. Mol. Struct.: THEOCHEM* **2002**, *589*, 125−137.
(52) Granier, T.; Thomas, E. L.; Gagnon, D. R.; Karasz, F. E.; Lenz, R. W. *J. Polym. Sci., Part B: Polym. Phys.* **1986**, *24*, 2793−2804.
(53) Chen, D.; Winokur, M. J.; Masse, M. A.; Karasz, F. E. *Polymer* **1992**, *33*, 3116−3122.
(54) Hu, D. H.; Yu, J.; Wong, K.; Bagchi, B.; Rossky, P. J.; Barbara, P. F. *Nature (London)* **2000**, *405*, 1030−1033.
(55) Pryamitsyn, V.; Ganesan, V. *J. Chem. Phys.* **2004**, *120*, 5824−5838.
(56) Holyst, R.; Oswald, P. *Macromol. Theory Simul.* **2001**, *10*, 1−16.
(57) Flory, P. J. *Principles of Polymer Chemistry*; Cornell University Press: Ithaca, NY, 1953.
(58) Walheim, S.; Boltau, M.; Mlynek, J.; Krausch, G.; Steiner, U. *Macromolecules* **1997**, *30*, 4995−5003.
(59) Pattison, L. R.; Hexemer, A.; Kramer, E. J.; Krishnan, S.; Petroff, P. M.; Fischer, D. A. *Macromolecules* **2006**, *39*, 2225−2231.
(60) Keil, M.; Rajagopal, A.; Yokoyama, S.; Sotobayashi, H.; Bradshaw, A. M.; Kakimoto, M. A.; Imai, Y. *Z. Phys. Chem., Int. J. Res. Phys. Chem. Chem. Phys.* **1997**, *202*, 87−102.
(61) Ettedgui, E.; Razafitrimo, H.; Gao, Y.; Hsieh, B. R.; Ruckman, M. W. *Synth. Met.* **1996**, *78*, 247−252.
(62) Mao, G.; Fischer, J. E.; Karasz, F. E.; Winokur, M. J. *J. Chem. Phys.* **1993**, *98*, 712−716.
(63) Gill, R. E.; Meetsma, A.; Hadziioannou, G. *Adv. Mater.* **1996**, *8*, 212.

MA060164L